In-Flight Calibration of the *Chandra* High Energy Transmission Grating Spectrometer

Herman L. Marshall, Daniel Dewey, and Kazunori Ishibashi

Center for Space Research, Massachusetts Institute of Technology, Cambridge, MA 02139

ABSTRACT

We present results from in-flight calibration of the High Energy Transmission Grating Spectrometer (HETGS) on the Chandra X-ray Observatory. Basic grating assembly parameters such as orientation and average grating period were measured using emission line sources. These sources were also used to determine the locations of individual CCDs within the flight detector. The line response function (LRF) was modeled in detail using an instrument simulator based on pre-flight measurements of the grating alignments and periods. These LRF predictions agree very well with in-flight observations of sources with narrow emission lines. Using bright continuum sources, we test the consistency of the detector quantum efficiencies by comparing positive orders to negative orders.

Keywords: Calibration, X-rays, Spectrometers

1. INTRODUCTION

We report on several sets of observations obtained with the *Chandra* High Energy Transmission Grating (HETG) to verify and measure various properties of the system. See Weisskopf et al. (2000,2002)[1,2] for an overview of the *Chandra* instrumentation and early results. The HETG is described in detail elsewhere[3,4] and in the *Chandra* Proposers' Observatory Guide.* Briefly, the HETG Spectrometer (HETGS) operates with the *Chandra* High Resolution Mirror Assembly (HRMA), which focusses X-rays through two sets of gratings in the HETG: high energy gratings (HEGs) with a period of 200.081 nm and the medium energy gratings (MEGs) with an average period of 400.141 nm. These disperse X-rays to the focal plane detector, which is usually the Advanced CCD Imaging Spectrometer (ACIS).[5]

Ground-based calibration observations have been previously reported[6–11] and are summarized in the HETGS Ground Calibration Report† These reports provide detailed ground-based measurements and modeling of various aspects of the HETGS such as the line response function (LRF) and the grating efficiencies. Here, we report on analysis of many observations obtained with the HETGS during in-flight calibration and instrument checkout.

The primary intent of these observations was to verify system performance using sources where some aspects are well understood. Many of the observations were obtained during the on-orbit activation and checkout (OAC), a two-week period in August, 1999 that began just after the ACIS detector door was opened. Others were obtained as part of a regular program to monitor the performance of the HETGS. Table 1 summarizes calibration data obtained and the use of these data sets. They are grouped according to the temperature of the focal plane detector (ACIS) and by observing cycle

Further author information: (Send correspondence to H.L.M.)
H.L.M.: E-mail: hermanm@space.mit.edu, Telephone: 1 617 253 8573

*Revision 5 of the Observatory Guide was published in December 2002 and is available on-line at `http://asc.harvard.edu/proposer/POG/index.html`.

†Available at `http://space.mit.edu/HETG/report.html`.

X-Ray and Gamma-Ray Instrumentation for Astronomy XIII, edited by Kathryn A. Flanagan, Oswald H. W. Siegmund, Proceedings of SPIE Vol. 5165 (SPIE, Bellingham, WA, 2004)
0277-786X/04/$15 · doi: 10.1117/12.508320

Table 1. HETGS Calibration Observations

Obsid(s)	Date(s)	Target	Comments
ACIS temperature = -100 C			
1098	8/28/99	Capella	HETGS First-light
1101, 1237	8/29/99	Capella	Focus set: "+0.2 mm"
1100, 1236	8/28/99	Capella	Focus set: "-0.2 mm"
1099, 1235	8/28/99	Capella	Focus set: "0.0 mm"
168, 169, 170	8/29/99	Crab Nebula	Effective Area and Timing
ACIS temperature = -110 C			
1103, 1318	9/24,25/99	Capella	Emission Line Project
1102	9/23-24/99	Cyg X-2	Effective Area
62538, 1252	9/14,17/99	HR 1099	Emission Line Project
457	11/5/99	Mkn 421	Effective Area
459	1/10/00	3C 273	Effective Area
ACIS temperature = -120 C			
1705	5/31/00	PKS 2155-304	Effective Area
1714	5/29/00	Mkn 421	Effective Area
57	3/3/00	Capella	Wavelength Stability
1014	3/28,29/01	PKS 2155-304	Effective Area
1010	2/11/01	Capella	Wavelength Stability
2463	6/13/01	3C 273	Effective Area
3167	11/30/01	PKS 2155-304	Effective Area
2583	4/29/02	Capella	Wavelength Stability
3456, 3457, 3573	6/5/02	3C 273	Effective Area and SIM offsets
3706, 3708	11/29/02	PKS 2155-304	Effective Area and SIM offsets
4430	7/7/03	3C 273	Effective Area

2. BASIC GRATING PARAMETERS

2.1. Grating Focus and Dispersion Axes

We analyed OAC observations of Capella at three different detector locations, x, along the focus direction (see Table 1) in order to locate the best focus, $\hat{x}$. The full width at half-maximum (FWHM) of an emission line along the dispersion direction varies quadratically with x:

$$\mathrm{FWHM}^2(x) = \mathrm{FWHM}^2_{\mathrm{min}} + C(x - \hat{x})^2 \quad (1)$$

where C is a constant related to the spectrometer geometry and $\mathrm{FWHM}_{\mathrm{min}}$ depends on the quality of the optics. Using eq. 1, we obtained $\hat{x}$ for each line and the zeroth order (Fig. 1). The zeroth order images in the data are heavily affected by pileup and not useful. Instead, the "trailed" (readout streak) events of the zeroth order were used. The best focus was $+0.077 \pm 0.028$ mm ($+0.049 \pm 0.041$ mm) for the dispersed MEG (HEG) emission lines. Thus, the overall HETG best-focus is in range of 0.050 to 0.100 mm with respect to the initial reference point (at step -505 of the Science Instrument Module [SIM] focus motor). Separate analyses by the imaging team yielded a best ACIS-S focus at 0.054 mm, so it was convenient and reasonable to set the HETGS focus at this same value (motor step -468).

The angles of the HEG and MEG spectra on the ACIS detector were measured using the Fe XVII 15 Å line, which is very bright in the observations of Capella, (observation IDs 1099 and 1235). The angles were measured as the slope of the line connecting the centers of the plus and minus first-order images of the line, giving $4.725 \pm 0.01°$ for the MEG and $-5.235 \pm 0.01°$ for the HEG. The angle between the dispersion lines is $9.96 \pm 0.01°$, which is consistent with the ground-based measurement of $9.93 \pm 0.01°$.

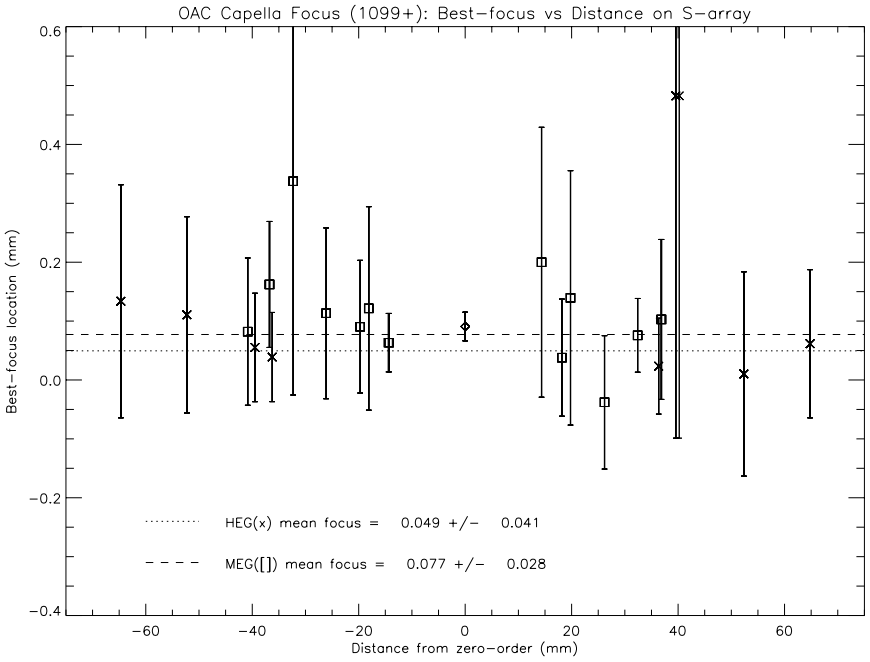

Figure 1. The best-focus location and uncertainty-range is shown for the zero-order (diamond) and a variety of HEG and MEG lines in Capella's spectra which cover a wide range along the ACIS-S detector. The adopted focus location of 0.054 mm is very close to the HEG best focus value determined here (dotted line.)

The FWHM of the 1D projection of the zeroth order readout streak for HETGS observations has been monitored for about four years. The width of the PSF can be broader for sources with harder spectra, so filtering on E <2 keV or E <3 keV has been applied in these cases, in order to provide a better comparison to other, softer sources. From Fig. 2, it is clear that the FWHM has been constant over this long baseline (with SIM focus motor still set at step -468). Note that these analyses included pixel randomization in the ACIS processing; the average FWHM value of 38.0 μm determined here is expected to be $\approx$34 μm when pixel randomization is eliminated.

2.2. Wavelength Accuracy

Relative wavelength accuracy is affected by the knowledge of the positions of the chips in the ACIS detector and accuracy of the dispersion scale, which is set by the HEG and MEG grating periods and the distance from the grating assembly to the focal plane. Lines are measured relative to zeroth order, taking out the uncertainties in the spacecraft attitude and telescope boresight.

2.2.1. ACIS Chip gaps

The ACIS-S detector is made up of six independant CCD detectors mounted in a line with approximately equal spacing. The geometry of each CCD is very well defined and stable but the five chip-to-chip offsets or gaps required calibration. To measure the gaps, we assume that an emission line observed on one side of the ACIS-S array should be measured to have the same wavelength when detected on the other side, that is $\lambda^+ = \lambda^-$. There is no assumption about the absolute line wavelength for this analysis, so even blended lines may be used. Any difference between these wavelengths is assumed to be due to a calibration error in the locations of the ACIS chips. Another term that is also included allows that the zeroth order for the HEG and MEG gratings (that is the corresponding HRMA shell pairs) may be offset from each other.

These offsets were measured in flight using emission lines from Capella, which is frequently observed for in-flight calibration. For each given line, some linear combination of the six parameters (5 chip gap values and

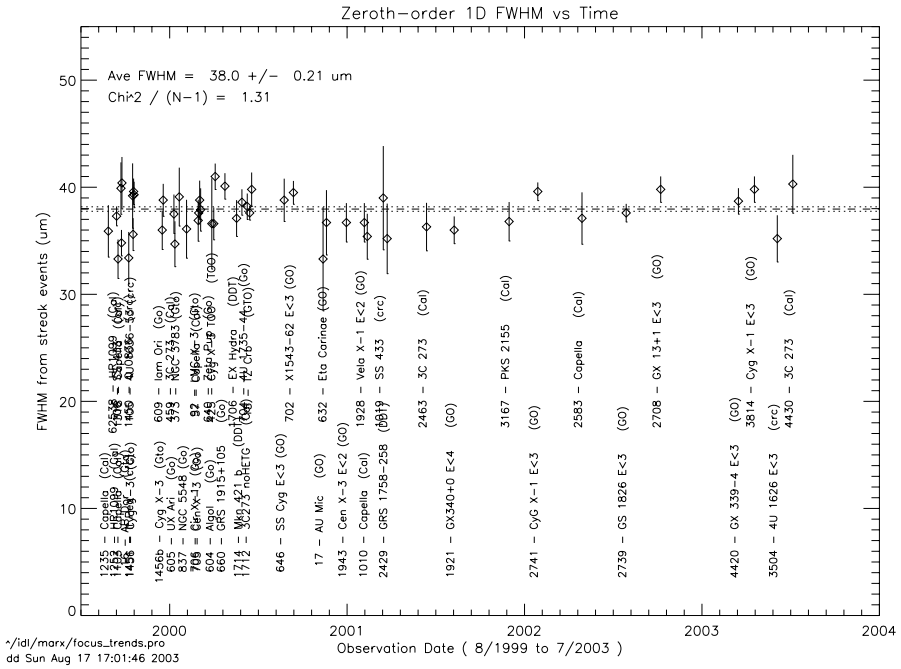

Figure 2. The full width at half-maximum (FWHM) of the readout streak for many bright sources as a function of observation date. For bright sources, the image is often heavily affected by pileup, so the readout streak is used, providing a 1D profile of the point spread function. The data are tightly distributed about an average of 38 μ ($\approx 0.8''$), showing that the focus has been stable for four years.

one HEG-MEG zeroth order offset) contributes to the difference between the measured wavelengths of the +1 and −1 orders. Lines are observed on many different chip combinations so all chip offsets can be determined. Six lines from the MEG spectra and five HEG lines were used: Si XIII at 6.6477Å, Mg XII (8.419 Å), Mg XI (9.1685 Å), Ne X (12.132 Å), Fe XVII (15.013 Å), and O VIII (18.967 Å). Singular value decomposition was used to solve this over-constrained set of linear equations (11 measurements for 6 parameters.)

Relative to the nominal design location of the CCDs, the in-flight determination of the chip gaps in September 1999 produced offsets to the chip locations in the "tiled detector" x (TDETX) coordinate of -4.97, -3.58, -2.42, 0, -0.08, and +0.33 pixels, for chips S0 to S5 respectively, where a pixel is about 0.024 mm. (Note that the offset of chip S3 is fixed at 0 by definition.) Capella was observed most recently in April 2002 and analyzed in a similar fashion to test for chip location changes. The analysis gave residual offsets from the above values, 0.53, 0.31, 0.20, 0, -0.03, and -0.23 pixels and an HEG-MEG zeroth-order offset value of 0.15 pixels. Using these changes to the offsets the overall wavelength residuals were of order 0.05 pixel (1σ). This shows that the chip offsets are stable and that re-analysis of the set of Capella observations could yield an offset calibration of order 0.1 pixel.

For reference, we note that the chip positions derived from pre-flight metrology indicated a set of offsets of -2.4, -2.1, -1.8, 0, -0.75, and -1.2 pixels. Later the locations were measured during the so-called molecular contamination tests taken when the telescope and flight ACIS detector were calibrated at the Marshall Space Flight Center's X-ray Calibration Facility; numerous emission lines due to contaminants on the C anode were measured. (Other results from these tests were reported by Marshall et al. 1998.[9]) Relative to ACIS chip S3, these tests yielded offsets of -3.4, -2.5, -1.9, 0, -0.3, and -0.6 pixels. We assign an uncertainty of 0.5 pixels due to chip location uncertainties.

2.2.2. Dispersion Scale and Overall Accuracy

After correcting for chip location errors, the absolute accuracy of wavelengths based on preflight instrument parameters was found to have a systematic fractional error of order 0.05% in the sense that measured wavelengths

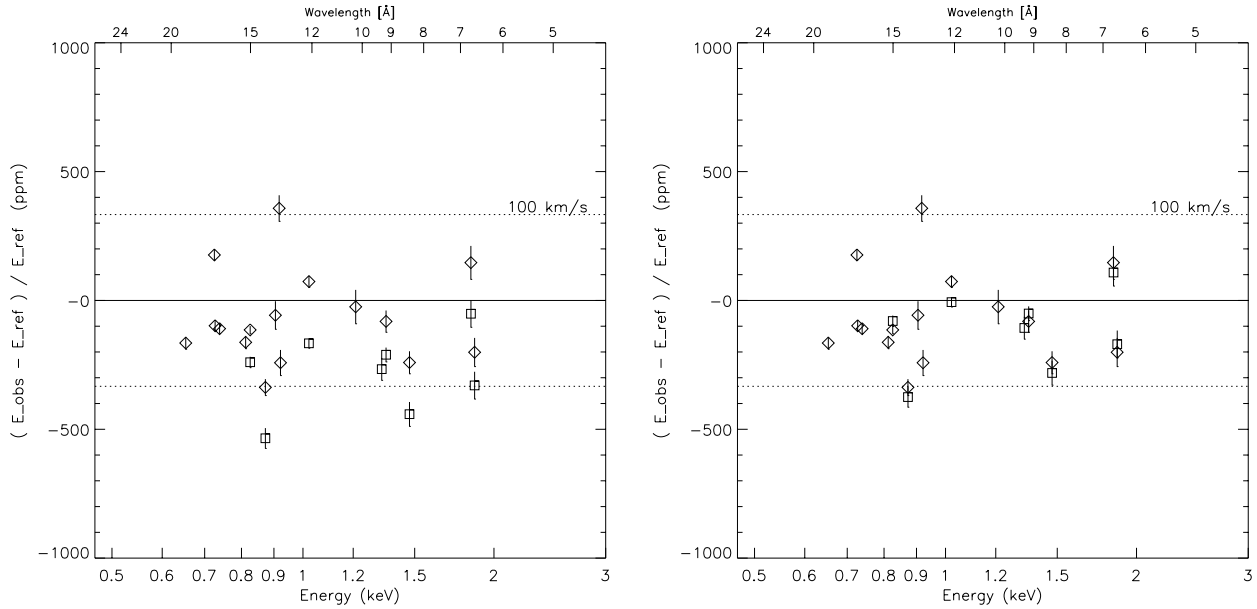

Figure 3. a) (Left) Measurements of lines in one observation of Capella (observation ID 2583). *Open squares:* Lines from the HEG portion of the spectrum. *Open diamonds:* Lines from the MEG portion of the spectrum. **b)** (Right) Same as fig. 3a) except that a correction of -0.016% has been applied to the HEG period, bringing the HEG wavelengths into better agreement with the MEG wavelengths. After correction, the average wavelength error would result in velocity errors of less than 100 km/s.

were too large. This difference was traced to a reduction in the ACIS-S pixel size from 24.000 microns to 23.987 microns as the detector substrate was cooled to the in-flight operating temperature of -120 C. This reduction was verified in preliminary analysis of calibration observations of the star cluster NGC 2516 by Maxim Markevitch. (The chip gap offsets, above, are unaffected by this scale change because they were measured using in-flight data.) After correcting for this scale error, MEG wavelengths show no systematic deviations from their expected values (Fig. 3) but the HEG wavelengths still show a systematic shift. This shift can be corrected by rescaling HEG wavelengths by -0.016%, corresponding to an HEG period of 200.049 nm. Thus, after applying these corrections, we estimate that the relative accuracy of wavelengths assigned to events on the basis of the distance from zeroth order appear to be good to better than 0.0055 Å (0.0028 Å) for MEG (HEG) spectra, limited primarily by the uncertainties in the ACIS chip locations.

3. HETGS LINE RESPONSE FUNCTION

The HETGS Line Response Function, LRF, consists of a Gaussian-like core and extended wings. The resolution of the spectrometer is specified by the FWHM of the core; the core plus wings are relevant to accurate line flux measurements. These properties are captured as resolution (or resolving power, E/dE) values and RMF files.

The results of ground testing of the HETG are incorporated into the ray-trace simulator, `MARX`.[12] The simulation software embodies much of the ground-calibration data, so line response functions are generated with millions of events and fitted with a model consisting of two Gaussian components and two Lorenztian components. The narrow Gaussian dominates the total power. The Lorentzian wings are rarely detectable in flight data, so they are fit to simulated data. The simulated event list was processed and fit using `IDL`^{TM}. The result is the expected HETGS LRF for a point source. An example of a very good fit is shown in fig. 4. The FWHM is well approximated by a cubic function of the wavelength:

$$\mathrm{FWHM} = c_0 + c_1\lambda + c_2\lambda^2 + c_3\lambda^3 \qquad (2)$$

Table 2. Coefficients for FWHM as a Function of λ (Eq. 2)

Grating	c_0	c_1	c_2	c_3
MEG	0.018851868	-0.00033946575	2.9781558e-05	-4.1097023e-07
HEG	0.010019662	-0.00014101982	1.4591413e-05	-1.9632994e-07

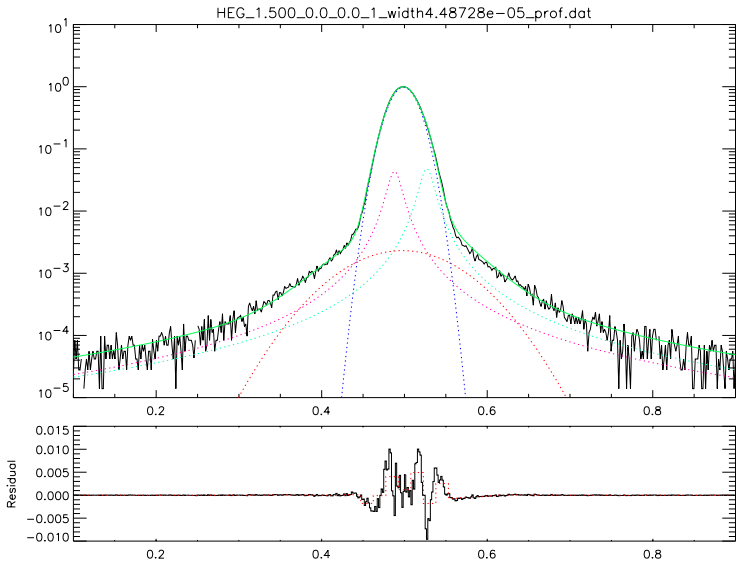

Figure 4. Example of a fit to an emission line generated using the `MARX` simulation software. The input line energy was 1.500 keV and only the HEG +1 order is shown. The line response function is modeled by two Gaussian components and two Lorenztian components. The narrow Gaussian dominates the total power. The Lorentzian wings are rarely detectable in flight data. The residuals (bottom panel) are largest in the core but are not statistically significant.

where c_i are given in table 2 for the MEG and HEG separately. The LRFs derived from the fits match the observed data from Capella (observation ID 1103) very well, as shown in figs. 5 and 6. More details are available on-line at `http://space.mit.edu/CXC/LSF/LSF_0002/`.

4. HETGS EFFECTIVE AREA

There are many components to the HETGS effective area model, specifically the HRMA, HETG, and ACIS. The focus here is on to ACIS-related effects that contribute important residuals to HETGS effective area calibration at this time. Using grating observations, we may test the validity of several components of the system without regard to the nature of the sources.

4.1. Comparing the BI and FI Quantum Efficiencies

Eighteen LETGS or HETGS observations were used to compare the quantum efficiencies (QEs) of backside-illuminated (BI) chips relative to frontside-illuminated (FI) chips. The observations were grouped approximately by date centered about January 2000, June 2000, January 2001, June 2001, and November, 2001. The data were extracted from L1 event lists processed using custom IDL scripts that have been used for other observations.[13–15] Briefly, the extraction region is 0.001° wide and the ACIS pulse height data were used to select events in wide regions that accept 95-99% of the events. All observations were obtained using ACIS in timed exposure (TE) mode except for one LETGS observation in continuous clocking (CC) mode. For the TE mode observations

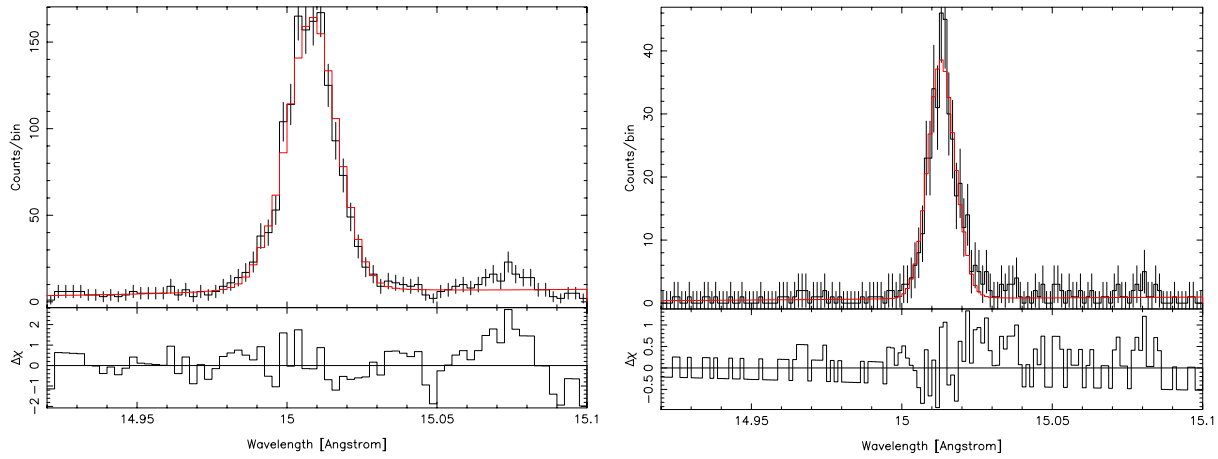

Figure 5. Comparison of data from Capella for the Fe XVII line at 15.013 Å to the LRF model fitted by the 4 component model shown schematically in Fig. 4. The left side compares the MEG data to the LRF model while the right side shows the same thing for the HEG data.

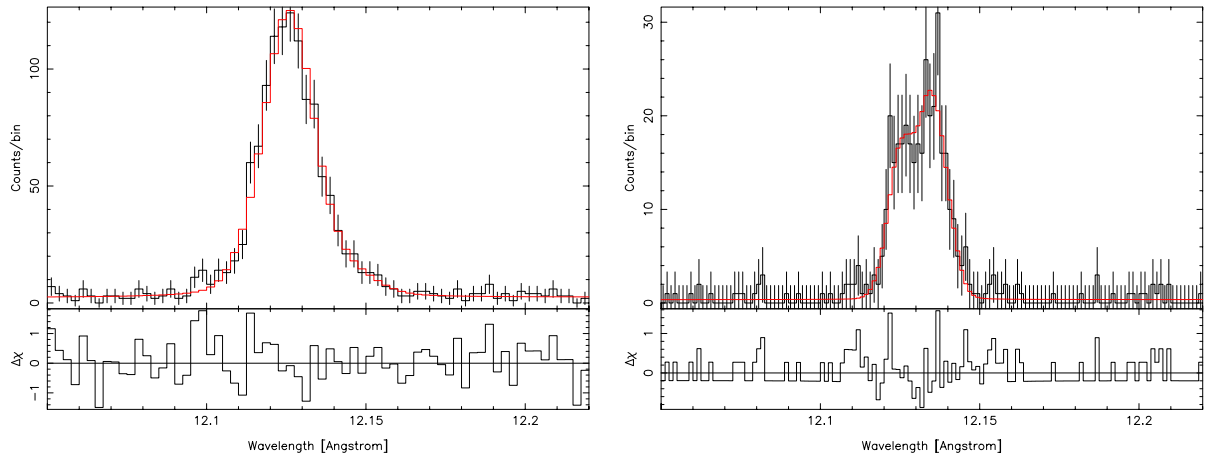

Figure 6. Same as in fig. 5 but for a blend of two lines. One is Fe XVII at 12.125 Å and the other is Ne X at 12.136 Å. The two lines are separated by 0.009 Å; they are not resolved by the MEG with an expected resolution of 0.018 Å at 12.13 Å but are marginally resolved by the HEG, for which the resolution is 0.0101 Å (using eq. 2) demonstrating that `MARX` provides very good simulations of the HETGS LRF.

background was selected from cross dispersion regions 0.003-0.01° from the dispersion line. For CC mode, background was taken from a pulse height region with equivalent range of E_{ACIS}/E_{OTG}.

The events identified with +1 and −1 orders were binned to about half of a spectral resolution element: 0.005 Å (HEG), 0.010 Å (MEG), and 0.025 Å (LETG). Background was binned similarly and subtracted after weighting by the ratio of the cross dispersion extraction widths. Uncertainties were computed from Poisson statistics for each bin. For each group of observations with net counts C_i^+ in the +1 order and C_i^- net counts in the −1 order and each grating, the ratio

$$R = \frac{Q^-}{Q^+} \frac{\sum_i C_i^+}{\sum_i C_i^-} \tag{3}$$

and its statistical uncertainty σ_R were computed over adaptively sized wavelength bins. Note that here we are assuming equality of plus and minus order efficiency for the gratings which is reasonable from ground tests and the random ±180° installation of grating facets in the HETG. The detector QEs on the +1 and −1 sides Q^+ and Q^-, are derived from the models of the CCDs in the detector and depend on wavelength. The index i indicates an individual observation in the group. Assuming that the QEs are not perfectly known, we assign $\hat{Q}^+$ and $\hat{Q}^-$ to represent the *true* QEs on these sides, so that the expected counts in each wavelength bin on the +1 and −1 sides are given by

$$C_i^+ = n_i A t \epsilon T \hat{Q}^+ d\lambda \tag{4}$$

$$C_i^- = n_i A t \epsilon T \hat{Q}^- d\lambda \tag{5}$$

where n_i is the source flux in ph cm^{-2} s^{-1} Å^{-1}, A is the effective area of the HRMA, t is the observation exposure, ϵ is the grating efficiency into first order, T is the transmission of the detector filter, Q^+ (Q^-) is the CCD efficiency on the +1 (−1) order side, and $d\lambda$ is the wavelength interval corresponding to one bin. All quantities are functions of wavelength except t. As defined, the quantity R is

$$R = \frac{Q^-}{Q^+} \frac{\hat{Q}^+}{\hat{Q}^-} \tag{6}$$

independent of the true and perhaps unknown source model, grating efficiency, or filter transmission. The bin wavelength limits, λ_1 to λ_2, were limited by $R/\sigma_R < 40$ and $\lambda_2 < 0.07\lambda_1$. In practice, there are very few observations for which the signal/noise is more than 40 over a small wavelength range. The bins have different sizes for each grating type.

The measurements of R are separated according to the type of CCD on the +1 and −1 sides to form a physically useful ratio

$$r = \frac{Q_{BI}/Q_{FI}}{\hat{Q}_{BI}/\hat{Q}_{FI}} \tag{7}$$

which gives the ratio of true QEs relative to the modeled QEs. If we have reason to believe that the the BI QEs are correct, for instance, then r gives the correction factor by which we multiply the modeled FI QEs to obtain the *true* QEs. The results are shown in fig. 7.

To check for time dependence, several wide wavelength intervals were averaged where r changes slowly. The ratios from different observations in similar time intervals were combined, where the time interval did not exceed 6 months. The results are shown in fig. 8. Limits to secular drifts are relatively stringent near 1 keV, $< 1\%$ change per year, and are somewhat larger at longer wavelengths: $< 10\%$ per year in the 20-25 Å range and $< 30\%$ per year in the 30-50 Å range.

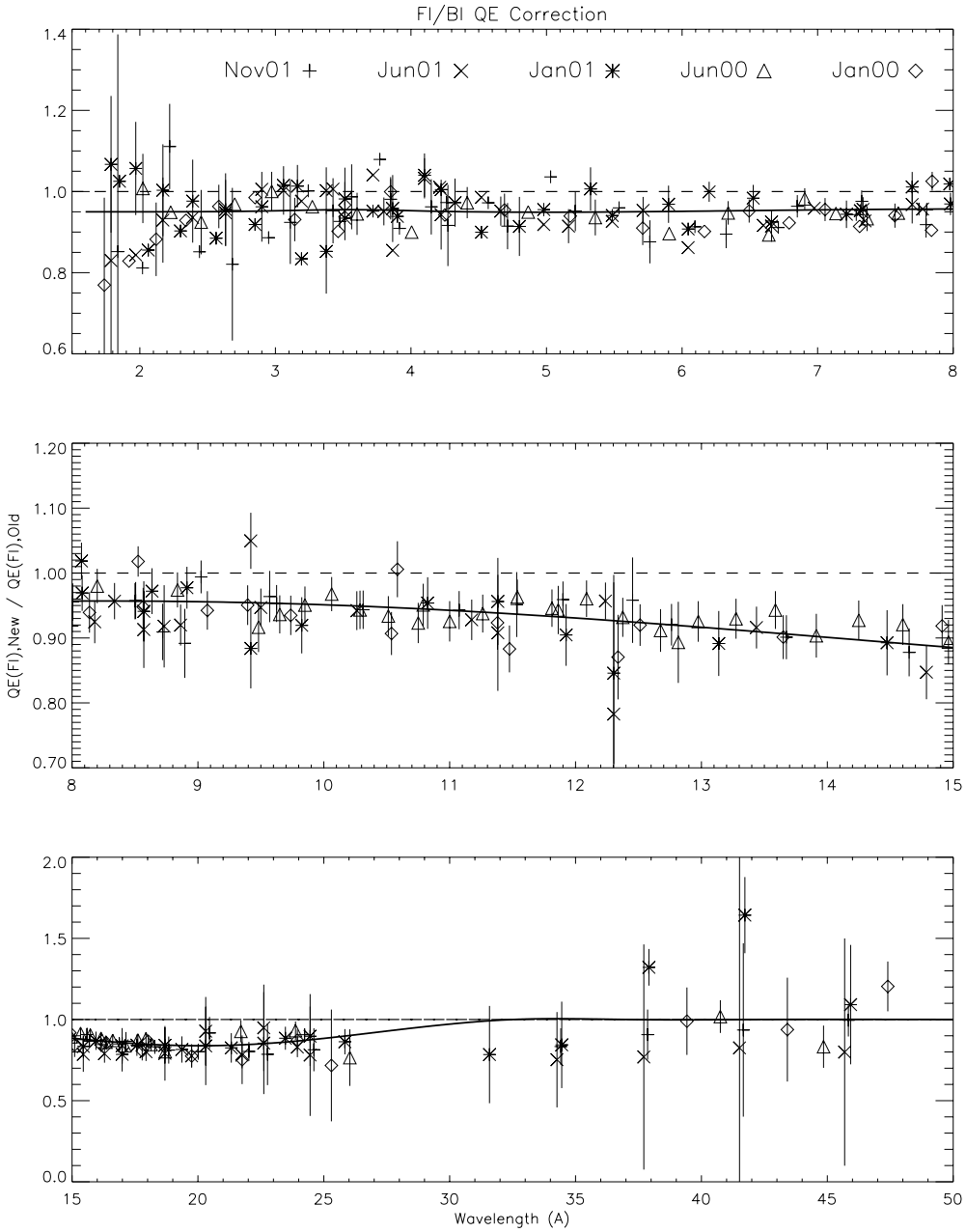

Figure 7. The ratio r as a function of wavelength for each observation set derived using eq. 7. The data are not segregated by grating type because the results are independent of the grating where comparisons are possible. All comparisons involving two FI chips gave R (eq. 6) consistent with 1 and are not shown. The heavy line is a polynomial fit to the data with Gaussian roll-off to the ends to avoid poor behavior of the polynomial extrapolation where the data are not as good.

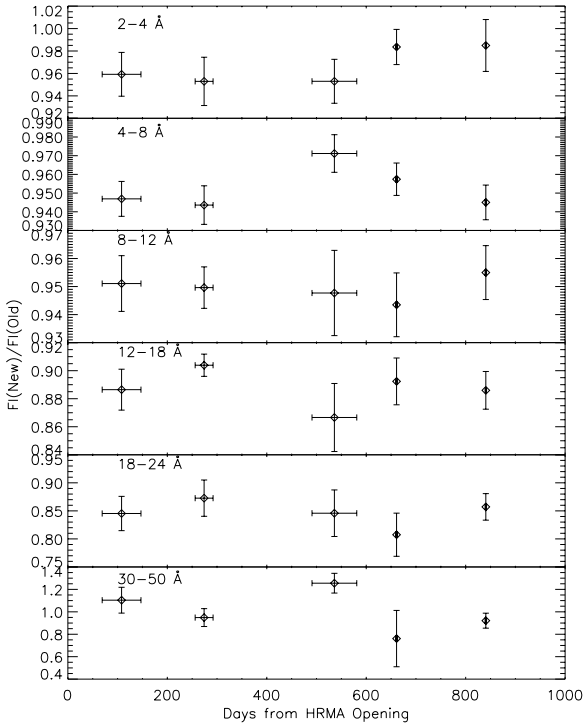

Figure 8. The data in fig. 7 were averaged over large wavelength regions due to the weak wavelength dependence and shown here as a function of observation time. The horizontal bars represent the time range of the observations within each group. These data are consistent with no change of the ratio of the QEs as a function of time. Limits to the secular trends have not been estimated but are rather small.

4.2. Accounting for Modest Pileup

Pileup is a highly non-linear effect that reduces the total counts selected for any specific grating order. Comparing the MEG and HEG spectra of the Crab pulsar shows what might happen. See the Proposers' Observatory Guide section 8.2.1.4 (particularly Fig. 8.14) for a detailed description of the effects of pileup in HETGS spectra. An empirical approach was used to make a first-order correction for pileup that reduces the effect of the Ir-M edge to a tolerable level.

A simple correction factor is applied to the effective areas based on the observed count spectrum. The event list is binned in the spectral dimension at a wavelength interval corresponding to one ACIS pixel (which depends on the grating), giving C_i, the counts in wavelength bin i. The total number of frames, N_f, is determined from the observation length and the frametime (less the framestore transfer time), giving the rate, $\rho_i = C_i/N_f$, in counts/frame in any given wavelength bin. The effective area correction is then

$$A' = Ae^{-a\rho_i} \tag{8}$$

for an FI chip or

$$A' = Ae^{-b\rho_i - c\rho_i^2} \tag{9}$$

for a BI chip. The coefficients a, b, and c were determined using an observation of XTE J1118-480 to be 7.5, 6.38, and 22.92. Note that the effective area is always reduced and that the correction factor drops rapidly with high count rates.

On a practical note, whenever there are few counts, the correction factor is discrete and the resultant correction factor will add noise. One way to avoid this problem is to use an averaging filter to determine the count rate for any given wavelength bin.

This approach has only been tested and seems to be effective for cases of mild to moderate pileup: rates less than about 0.1-0.2 count/frame/bin. For more extreme cases, a more detailed model is necessary. One method is described by Davis (2001,2003).[16,17] ‡

4.3. Overall Effective Area Reliability

Based on the results from the HETGS calibration observations of the Crab pulsar and Mk 421 we place the following estimates on the systematic uncertainties of HETGS spectral fluxes, after correcting for the system effective area using the currently released calibration data products: 10% for $1.5 < E < 6$ keV (both MEG and HEG), 20% for $6 < E < 8$ keV (HEG only), 20% in the Si-K edge region (1.83-1.84 keV) (both MEG and HEG), 20% for $0.8 < E < 1.5$ keV (both MEG and HEG), 30% for $0.5 < E < 0.8keV$ (MEG only), 50% in the O-K edge region (0.525-0.57 keV) (MEG only). Except for the last two regions, one may conservatively use 10% for $E > 2$ keV and 20% for $E < 2$ keV except in the edge regions. The MEG is probably better than 20% in the 0.5-0.8 keV region but the data are not conclusive. The quoted uncertainties are meant to give the uncertainty on fluxes determined in one band relative to those in another band. Absolute flux uncertainties have not yet been verified but are expected to be good to a better than 5-10%. The uncertainties include systematic errors in many instrument components, including the HETGS efficiencies and ACIS filter and QE models, and are meant to reflect the system performance.

5. SUMMARY AND FUTURE WORK

On the whole, the HETGS performs as expected in flight and in-flight calibrations are merely fine adjustments to ground-based initial values. In this paper we've presented some of the more important and unique HETGS calibration activities carried out using flight data. In many cases, these calibrations have been captured in the calibration data products used by processing software. In several cases these calibrations are in process and will show up in the calibration products in the near future.

ACKNOWLEDGMENTS

We acknowledge and thank our many Chandra collegues. This work was supported in part by the Smithsonian Astrophysical Observatory (SAO) contract SVI-61010 for the Chandra X-Ray Center (CXC) and by NASA through contract NAS8-01129.

REFERENCES

1. M. C. Weisskopf, H. D. Tananbaum, L. P. Van Speybroeck, and S. L. O'Dell, "Chandra X-ray Observatory (CXO): overview," in *Proc. SPIE Vol. 4012, p. 2-16, X-Ray Optics, Instruments, and Missions III, Joachim E. Truemper; Bernd Aschenbach; Eds.*, pp. 2–16, July 2000.
2. M. C. Weisskopf, B. Brinkman, C. Canizares, G. Garmire, S. Murray, and L. P. Van Speybroeck, "An Overview of the Performance and Scientific Results from the Chandra X-Ray Observatory," *PASP* **114**, pp. 1–24, Jan. 2002.
3. C. R. Canizares, M. L. Schattenburg, and H. I. Smith, "The high energy transmission grating spectrometer for AXAF," in *X-ray instrumentation in astronomy; Proceedings of the Meeting, Cannes, France, December 2-4, 1985 (A87-19722 07-35). Bellingham, WA, Society of Photo-Optical Instrumentation Engineers, 1986, p. 253-260.*, pp. 253–260, 1986.
4. T. H. Markert, C. R. Canizares, D. Dewey, M. McGuirk, C. S. Pak, and M. L. Schattenburg, "High-Energy Transmission Grating Spectrometer for the Advanced X-ray Astrophysics Facility (AXAF)," in *Proc. SPIE Vol. 2280, p. 168-180, EUV, X-Ray, and Gamma-Ray Instrumentation for Astronomy V, Oswald H. Siegmund; John V. Vallerga; Eds.*, pp. 168–180, Sept. 1994.

‡See also the web page `http://space.mit.edu/CXC/analysis/PILECOMP/index.html`.

5. G. P. Garmire, M. W. Bautz, P. G. Ford, J. A. Nousek, and G. R. Ricker, "Advanced CCD imaging spectrometer (ACIS) instrument on the Chandra X-ray Observatory," in *X-Ray and Gamma-Ray Telescopes and Instruments for Astronomy. Edited by Joachim E. Truemper, Harvey D. Tananbaum. Proceedings of the SPIE, Volume 4851, pp. 28-44 (2003).*, pp. 28–44, Mar. 2003.
6. D. Dewey, K. A. Flanagan, H. L. Marshall, C. Baluta, C. R. Canizares, D. S. Davis, J. E. Davis, T. T. Fang, D. P. Huenemoerder, J. H. Kastner, N. S. Schulz, M. W. Wise, J. J. Drake, J. Z. Juda, M. Juda, A. C. Brinkman, C. J. Gunsing, J. S. Kaastra, G. D. Hartner, and P. Predehl, "Toward the calibration of the HETGS effective area," in *Proc. SPIE Vol. 3113, p. 144-159, Grazing Incidence and Multilayer X-Ray Optical Systems, Richard B. Hoover; Arthur B. Walker; Eds.*, pp. 144–159, July 1997.
7. H. L. Marshall, D. Dewey, K. A. Flanagan, C. Baluta, C. R. Canizares, D. S. Davis, J. E. Davis, T. T. Fang, D. P. Huenemoerder, J. H. Kastner, N. S. Schulz, M. W. Wise, J. J. Drake, J. Z. Juda, M. Juda, A. C. Brinkman, C. J. Gunsing, J. S. Kaastra, G. D. Hartner, and P. Predehl, "Toward the calibration of the HETGS line response function," in *Proc. SPIE Vol. 3113, p. 160-171, Grazing Incidence and Multilayer X-Ray Optical Systems, Richard B. Hoover; Arthur B. Walker; Eds.*, pp. 160–171, July 1997.
8. D. Dewey, J. J. Drake, R. J. Edgar, K. Michaud, and P. Ratzlaff, "AXAF grating efficiency measurements with calibrated nonimaging detectors," in *Proc. SPIE Vol. 3444, p. 48-63, X-Ray Optics, Instruments, and Missions, Richard B. Hoover; Arthur B. Walker; Eds.*, pp. 48–63, Nov. 1998.
9. H. L. Marshall, D. Dewey, N. S. Schulz, and K. A. Flanagan, "Spectral features in the AXAF HETGS effective area using high-signal-continuum tests," in *Proc. SPIE Vol. 3444, p. 64-75, X-Ray Optics, Instruments, and Missions, Richard B. Hoover; Arthur B. Walker; Eds.*, pp. 64–75, Nov. 1998.
10. J. E. Davis, H. L. Marshall, D. Dewey, and M. L. Schattenburg, "Analysis and modeling of anomalous scattering in the AXAF HETGS," in *Proc. SPIE Vol. 3444, p. 76-92, X-Ray Optics, Instruments, and Missions, Richard B. Hoover; Arthur B. Walker; Eds.*, pp. 76–92, Nov. 1998.
11. N. S. Schulz, D. Dewey, and H. L. Marshall, "Absolute effective areas of the HETGS," in *Proc. SPIE Vol. 3444, p. 160-176, X-Ray Optics, Instruments, and Missions, Richard B. Hoover; Arthur B. Walker; Eds.*, pp. 160–176, Nov. 1998.
12. M. W. Wise, D. P. Huenemoerder, and J. E. Davis, "Simulated AXAF Observations with MARX," in *ASP Conf. Ser. 125: Astronomical Data Analysis Software and Systems VI*, pp. 477–+, 1997.
13. H. L. Marshall, R. Rutledge, D. W. Fox, J. M. Miller, R. Guerriero, E. Morgan, M. van der Klis, L. Bildsten, T. Dotani, and W. H. G. Lewin, "X-Ray Spectrum of the Rapid Burster Using the Chandra HETGS," *AJ* **122**, pp. 21–25, July 2001.
14. H. L. Marshall, C. R. Canizares, and N. S. Schulz, "The High-Resolution X-Ray Spectrum of SS 433 Using the Chandra HETGS," *ApJ* **564**, pp. 941–952, Jan. 2002.
15. J. E. McClintock, C. A. Haswell, M. R. Garcia, J. J. Drake, R. I. Hynes, H. L. Marshall, M. P. Muno, S. Chaty, P. M. Garnavich, P. J. Groot, W. H. G. Lewin, C. W. Mauche, J. M. Miller, G. G. Pooley, C. R. Shrader, and S. D. Vrtilek, "Complete and Simultaneous Spectral Observations of the Black Hole X-Ray Nova XTE J1118+480," *ApJ* **555**, pp. 477–482, July 2001.
16. J. E. Davis, "Event Pileup in Charge-coupled Devices," *ApJ* **562**, pp. 575–582, Nov. 2001.
17. J. E. Davis, "Pile-up model for dispersed spectra," in *X-Ray and Gamma-Ray Telescopes and Instruments for Astronomy. Edited by Joachim E. Truemper, Harvey D. Tananbaum. Proceedings of the SPIE, Volume 4851, pp. 101-111 (2003).*, pp. 101–111, Mar. 2003.